Journal of Asian Earth Sciences 36 (2009) 289–302

Contents lists available at ScienceDirect

Journal of Asian Earth Sciences

journal homepage: www.elsevier.com/locate/jseaes

Radial anisotropy in the crust and upper mantle beneath the Qinghai-Tibet Plateau and surrounding regions

Yun Chen [a,*], José Badal [b], Zhongjie Zhang [a]

[a] State Key Laboratory of Lithospheric Evolution, Institute of Geology and Geophysics, Chinese Academy of Sciences, Beijing 100029, PR China
[b] Physics of the Earth, Sciences B, University of Zaragoza, Pedro Cerbuna 12, 50009 Zaragoza, Spain

ARTICLE INFO

Article history:
Received 11 June 2008
Received in revised form 21 February 2009
Accepted 9 June 2009

Keywords:
Surface waves
Tomography
Radial anisotropy
Qinghai-Tibet Plateau

ABSTRACT

Relative SV and SH wave speeds are generally attributed to radial seismic anisotropy which can be used as the indicator of crust/mantle deformation styles. Surface wave data were initially collected from events of magnitude Ms $\geqslant$ 5.0 and shallow or moderate focal depth occurring between 1980 and 2002: 713 of them generated Rayleigh waves and 660 Love waves, which were recorded by 13 broadband digital stations in Eurasia and India. Up to 1525 source-station Rayleigh waveforms and 1464 Love wave trains were earlier analysed by multiple filtering to obtain Love- and Rayleigh wave group velocity curves in the broad period range 10–105 s. We have performed tomographic inversion to obtain period-dependent group velocity and further shear wave velocity at $2^\circ \times 2^\circ$-sized grid-cells of a mesh covering the model region, after averaging azimuthal effects. Horizontally and vertically varying shear-wave velocities are observed, but the models of isotropic seismic velocity in the crust and upper mantle cannot fit simultaneously the inverted group-velocity dispersion curves due to the discrepancy in the transmission velocities of Love and Rayleigh waves, whose likely origin is the existence of radial anisotropy in the continental crust and topmost mantle. The strength of radial anisotropy computed from the Love–Rayleigh discrepancy and its spatial extent beneath the Qinghai-Tibet Plateau are shown as maps of percentage anisotropy at various depths down to 170 km and cross-sections along five profiles of reference. Areas in which radial anisotropy is in excess of $\sim$ 6% are found in the crust and upper mantle underlying most of the plateau, and even up to 10% in some places. The strength and spatial configuration of radial anisotropy seem to indicate the existence of a regime of horizontal compressive forces in the frame of the convergent Himalayan–Tibetan orogen, the laterally variation of the lithospheric rheology and the differential movement as regards the compressive driving forces.

1. Introduction

Deformation in the crust and mantle induces a fabric which is a likely cause of seismic anisotropy, i.e. the dependence of local wave propagation characteristics on the direction and polarization of the seismic wavefield. Therefore, the determination of seismic anisotropy in the Earth's interior provides essential clues to understand the Earth's dynamic evolution (Fouch and Rondenay, 2006; Maggi et al., 2006). Seismic anisotropy causes many diverse effects, these include azimuthal variation of *Pn* velocities, shear-wave splitting in teleseismic *SKS* waves. Seismic anisotropy also leads to Love and Rayleigh wave velocity dispersion that differ significant from those associated with propagation in isotropic media. Surface waves as a useful tool for the investigation of the Earth's anisotropic properties was advanced by Anderson (1961). Shear wave velocities derived from Love waves assuming isotropic propagation often differ from those derived from Rayleigh waves under the same isotropic assumption. Such incompatibilities are generally considered as a robust diagnostic for the presence of anisotropy in the crust and upper mantle, which is commonly called radial or polarization anisotropy (Ekström and Dziewonski, 1998; Debayle and Kennett, 2000; Muyzert and Snieder, 2000), and this evidence led to the early compilation of a global 1D reference Earth model with 2–4% of radial anisotropy in the mantle down to 220 km (Dziewonski and Anderson, 1981).

Global seismic anisotropy has been detected by Montagner and Tanimoto (1990, 1991), Park and Levin (2002), and Shapiro and Ritzwoller (2002); and anisotropy in limited regions has been reported by Montagner and Jobert (1988), Ribe (1989), Ekström and Dziewonski (1998), Silveira et al. (1998), Ritzwoller et al. (2001), Villaseñor et al. (2001), Meissner et al. (2002), Raykova and Nikolova (2003), and Marone et al. (2004). Some evidences for anisotropy in the specific area of Tibet has been reported by Song et al. (1991), Lavé et al. (1996), Huang et al. (2004), Ozacar and Zandt (2004), Shapiro et al. (2004), and Lev et al. (2006). Much

* Corresponding author. Tel.: +86 10 82998331.
E-mail address: yunchen@mail.iggcas.ac.cn (Y. Chen).

1367-9120/$ - see front matter © 2009 Elsevier Ltd. All rights reserved.
doi:10.1016/j.jseaes.2009.06.011

effort has been devoted to estimate differences between SH-wave velocity and SV-wave velocity both regionally (Villaseñor et al., 2001) and globally (Shapiro and Ritzwoller, 2002). Anyhow, the robust estimation of these velocities is much more difficult than estimating isotropic shear velocity as the use of different subsets of data affects estimates of the strength of radial anisotropy (Ritzwoller et al., 2001).

Radial anisotropy can only be resolved unambiguously by incorporating short and intermediate period measurements in the starting surface wave data set. In this paper we supply an overall view of strength and distribution of radial anisotropy in the Qinghai-Tibet Plateau and adjacent areas contoured by latitudes 22–44°N and longitudes 70–106°E (Fig. 1), which is an ideal place for the study of the geological evolution of the Himalayan–Tibetan orogen (Yin and Harrison, 2000).

2. Dataset

The test region is monitored by 13 broadband digital stations installed in Eurasia and India, and this network consists of: 6 belonging to the China Digital Seismograph Network (CDSN), later included in the IRIS China Digital Seismograph Network (ICDSN), 4 to the Global Seismograph Network (GSN), 2 to the GEOSCOPE Network and 1 to the Seismic Research Observatory (SRO). We picked up 713 events for Rayleigh waves and 660 events for Love waves during the period January 1980 to December 2002. These Asian earthquakes registered by the arrays have magnitude Ms $\geqslant$ 5.0 (around 94% between 5.0 and 6.0) and focal depth < 100 km (around 80% less than 50 km), and all of them generated surface waves in the broad period range 10–105 s but with high signal-to-noise ratio at intermediate periods (10–70 s). Both the vertical component and the two horizontal components of the Rayleigh and Love motion were corrected for instrument response and their respective traces reduced to ground motion.

We chose as many stations and events as possible in an effort to collect a great number of regional ray-paths sampling the area, thus minimizing the impact of diffraction-related errors and undesirable contributions coming from outside velocity anomalies. Moreover, in order to minimize data redundancy and off-great-circle propagation effects, those paths with nearby azimuth are considered to be similar if their starting and ending points both lie within 1.5% of the path-length from one another. In both cases we have a dense and more or less uniform coverage with waves travelling in all azimuths and sampling a variety of physiographic regions. Segment lengths in percentage of the total path falling into the five tectonic provinces that form the main body of the Qinghai-Tibet Plateau reach the 75%. Lastly, we collected up to 1525 source-station Rayleigh waveforms and 1464 source-station Love wave trains propagating along great-circle paths, which lengths range between 800 and 4000 km and the period-dependent average path-length is about 2000 km. Fig. 2 shows the ray-path coverage (source-receiver straight lines) at 50 s period for Love and Rayleigh waves across the study area. Within the available bandwidth, the crust and uppermost mantle are well sampled by fundamental mode Love- and Rayleigh waves.

3. Method

3.1. Group-velocity dispersion curves

To minimize possible errors due to higher mode interference, scattering coda and noise, moving-window analysis was used on

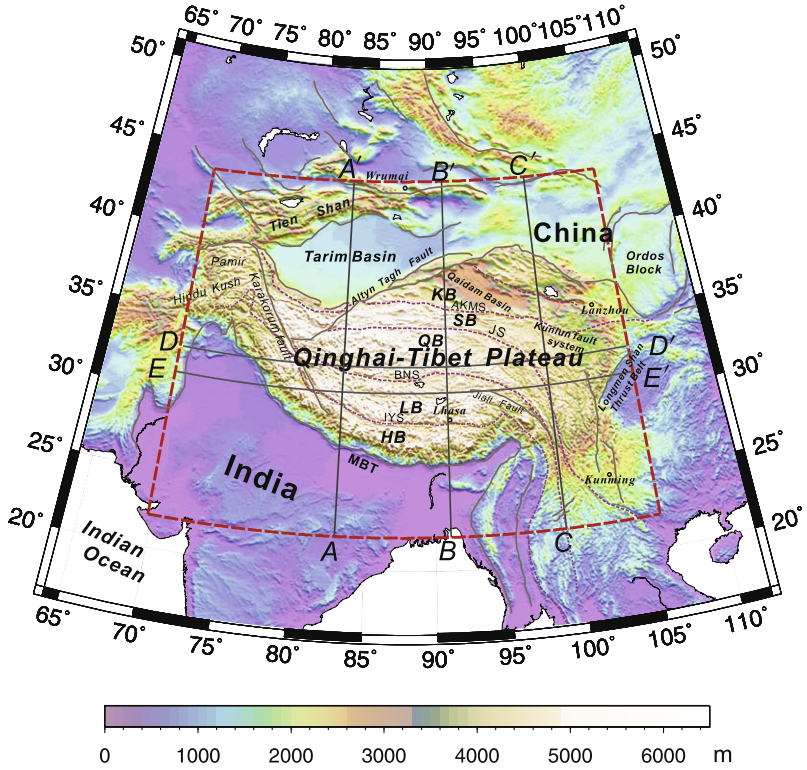

Fig. 1. Setting map of the Qinghai-Tibet Plateau and surrounding areas outlined by a dash line (22–44°N, 70–106°E). Tectonic lines depicted after Yin and Harrison (2000). Key to symbols: MBT, Main Boundary Thrust; IYS, Indus-Yalu Suture; BNS, Bangong-Nujiang Suture; JS, Jinsha Suture; AKMS, Ayimaqin-Kunlun-Mutztagh Suture; HB, Himalayan Block; LB, Lhasa Block; QB, Qiangtang Block; SB, Songpan-Ganzi Block; KB, Kunlun-Qaidam Block. Transects A–A′, B–B′ and C–C′ mark N–S vertical cross-sections along 83°, 91° and 99° of east longitude, which cross western, central and eastern Tibet, respectively; profiles D–D′ and E–E′ mark E–W vertical cross-sections along 33° and 31° of north latitude, which cross the Qiangtang and Lhasa Blocks, respectively.

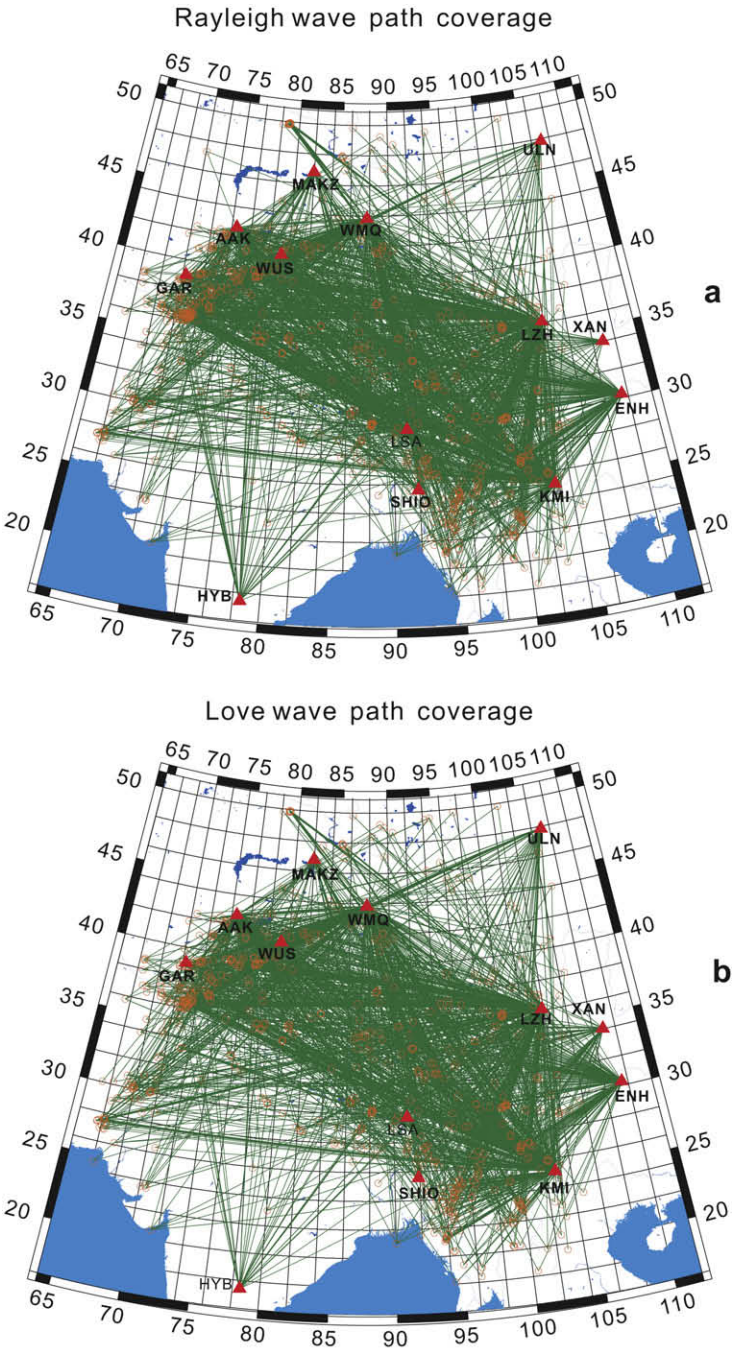

Fig. 2. Ray-path coverage (source-receiver straight lines) for 50 s Rayleigh (a) and Love (b) waves propagating across the study area. Triangles and circles mark geographical locations of seismic stations and events, respectively.

each seismic signal to measure with least possible bias the dispersion of every selected wave train (Badal et al., 1990, 1992). The Rayleigh wave group-velocity dispersion curve was obtained by applying a narrow bandwidth Gaussian filter to the ground-motion vertical component over different periods (Pasyanos and Walter, 2001). Similarly, Love dispersion measurements were obtained by applying the same filter to the data rotated and converted into transverse motion (Raykova and Nikolova, 2003). Frequency–time analysis of the fundamental mode Love and Rayleigh waves to obtain group velocity from the dispersed wave trains was carried out using the software developed by Herrmann (2002). In order to minimize data redundancy and off-great-circle propagation effects, those paths with nearby azimuths were considered to be similar if their starting and ending points both lie within 1.5% of the path-length from one another. Clustering is useful to estimate the frequency-dependent standard deviation of the measurements within each cluster and to estimate the frequency-dependent standard deviation of the entire dataset (Ritzwoller and Levshin, 1998; Vuan et al., 2005). In all cases the velocity values exhibit a similar amount of scatter and are inside a narrow standard deviation band that does not exceed 0.02 km/s at the most.

3.2. Tomographic inversion

Two-step tomographic inversion of Rayleigh and Love wave dispersion data was used to obtain local group-velocity dispersion

and then SV- and SH-wave velocity structure beneath the Qinghai-Tibet Plateau and adjacent areas. First, inverting the path-averaged group times by means of a tomographic method based on the stochastic scheme (Aki and Richards, 1980; Dimri, 1992), we retrieved location-dependent group velocities on a $2^\circ \times 2^\circ$-sized grid at periods from 10.4 to 105.0 s for Rayleigh and Love waves (Chen et al., 2009). A series of reliability assessments, which included the computation of the covariance and resolution matrices, resolving kernels and several sparse-spike tests were carried out, and the results demonstrated that the true resolution that can be claimed for the study region is about 200 km. Second, damped least-squares were applied to invert point-by-point the previous local dispersion curves for SV- and SH-wave velocity structure of the crust and upper mantle (Chen et al., 2009). We used damped least-squares

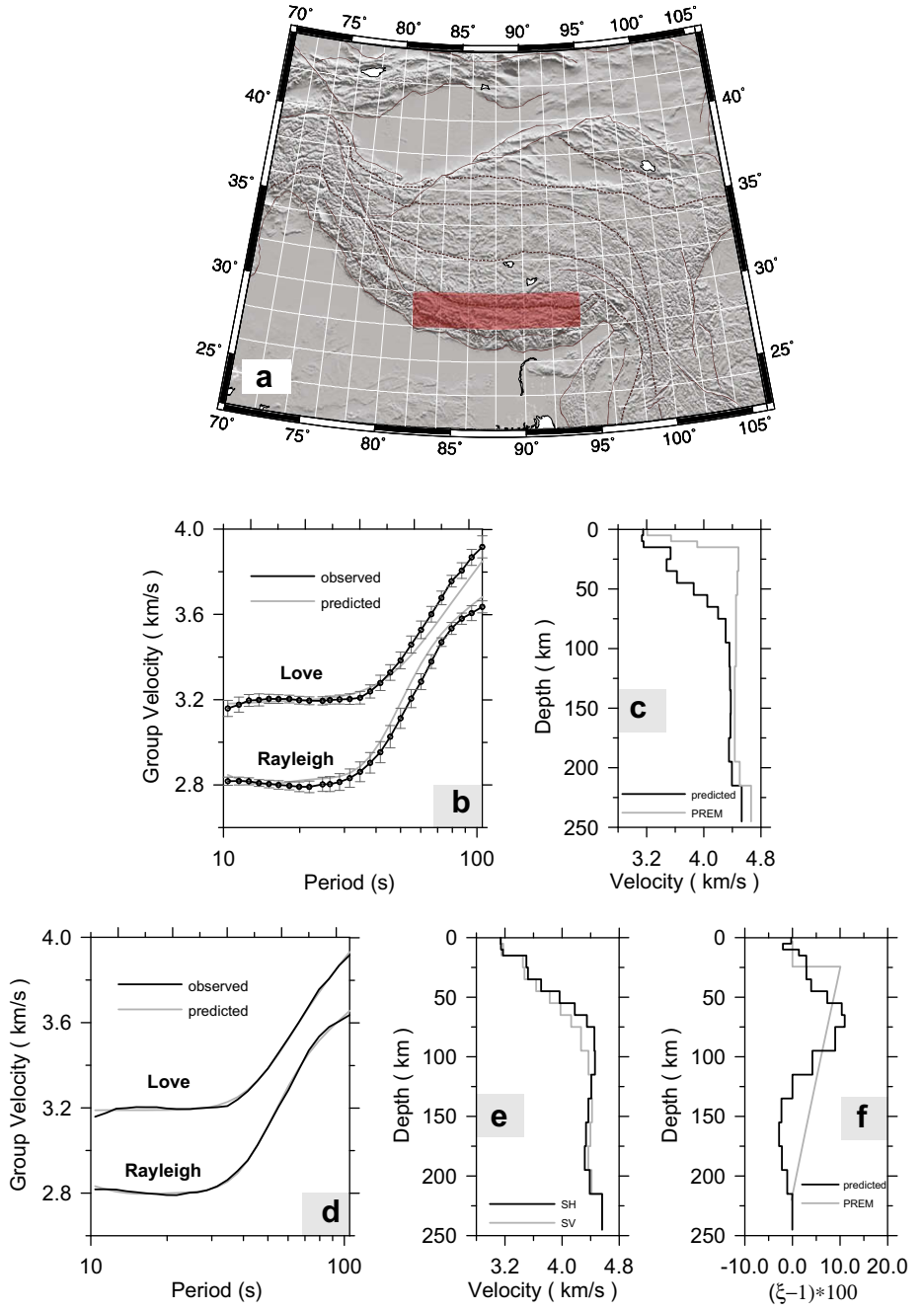

Fig. 3. Radial anisotropy features in the crust and upper mantle of the Himalayan Block. (a) Location map shown the grid-cells with size of $2^\circ \times 2^\circ$ (masked by red colour) we used to average the Love and Rayleigh wave group-velocity dispersion of a tectonic unit. The grid-cells are consistent with the regionalization in the inversion of group-velocity dispersion. (b) Simultaneous fit to the observed, averaged Love and Rayleigh wave group-velocity dispersion curves by forward modelling from the isotropic, elastic depth-dependent S-velocity model (black line) shown in (c). The standard deviations (vertical error bars) are inferred from the group velocity variance on $2^\circ \times 2^\circ$ cells almost within the same tectonic unit shown in (a). The observed dispersion curves are drawn by black lines, while the predicted (theoretical) dispersion curves are drawn by grey lines and they correspond to the best-fitting crust–mantle model plotted in (d). The starting model is the isotropic PREM model (grey line) also included in (c) as reference. (d) Group-velocity dispersion fitting from the crust–mantle SH- and SV-wave velocity models shown in (e). The overlap between observed and predicted dispersion is now excellent. (f) Predicted strength of radial anisotropy in the crust and upper mantle from the incompatibility between the best-fitting V_{SH} and V_{SV} velocity models shown in (e). Here the strength of radial anisotropy is defined as $(\xi - 1) * 100$, being $\xi = (V_{SH}/V_{SV})^2$. The variation of anisotropy with depth (grey line) as derived from the anisotropic PREM model has also been included for comparison. (For interpretation of the references to colour in this figure legend, the reader is referred to the web version of this article.)

inversion (Russell, 1987; Julià et al., 2000; Herrmann, 2002; Rapine et al., 2003) to determine the best-fitting shear velocity model, so that SV- and SH-wave velocities were obtained at each node of the $2^\circ \times 2^\circ$ grid. Kernels of the resolution matrix were computed at various reference depths and target grid nodes to estimate the quality of the solution, and the results showed that the resolvable depth by Rayleigh waves is ~220 km, and ~170 km by Love waves.

3.3. Retrieving radial anisotropy

Theoretically, in an isotropic medium the SH-wave velocity (V_{SH}) and the SV-wave velocity (V_{SV}) are equal, but they differ in an anisotropic material. In other words, the Rayleigh and Love dispersion curves can be well fitted simultaneously by the same 1D isotropic, elastic depth-dependent shear-wave velocity model in an isotropic medium. However, when horizontally polarized Love waves and vertically polarized Rayleigh waves propagate with distinct speeds ($V_{SH} \neq V_{SV}$), the Love–Rayleigh (L–R) discrepancy can be explained in terms of transverse isotropy of the elastic medium (Lévêque et al., 1998; Debayle and Kennett, 2000; Muyzert and Snieder, 2000; Silveira and Stutzmann, 2002; Raykova and Nikolova, 2003; Marone et al., 2004; Fouch and Rondenay, 2006). In a previous paper (Chen et al., 2009), we computed averaged Rayleigh and Love wave group-velocity dispersion curves for each main tectonic unit of the Tibetan Plateau from the local group velocities determined on each $2^\circ \times 2^\circ$ grid-cell falling into the target tectonic

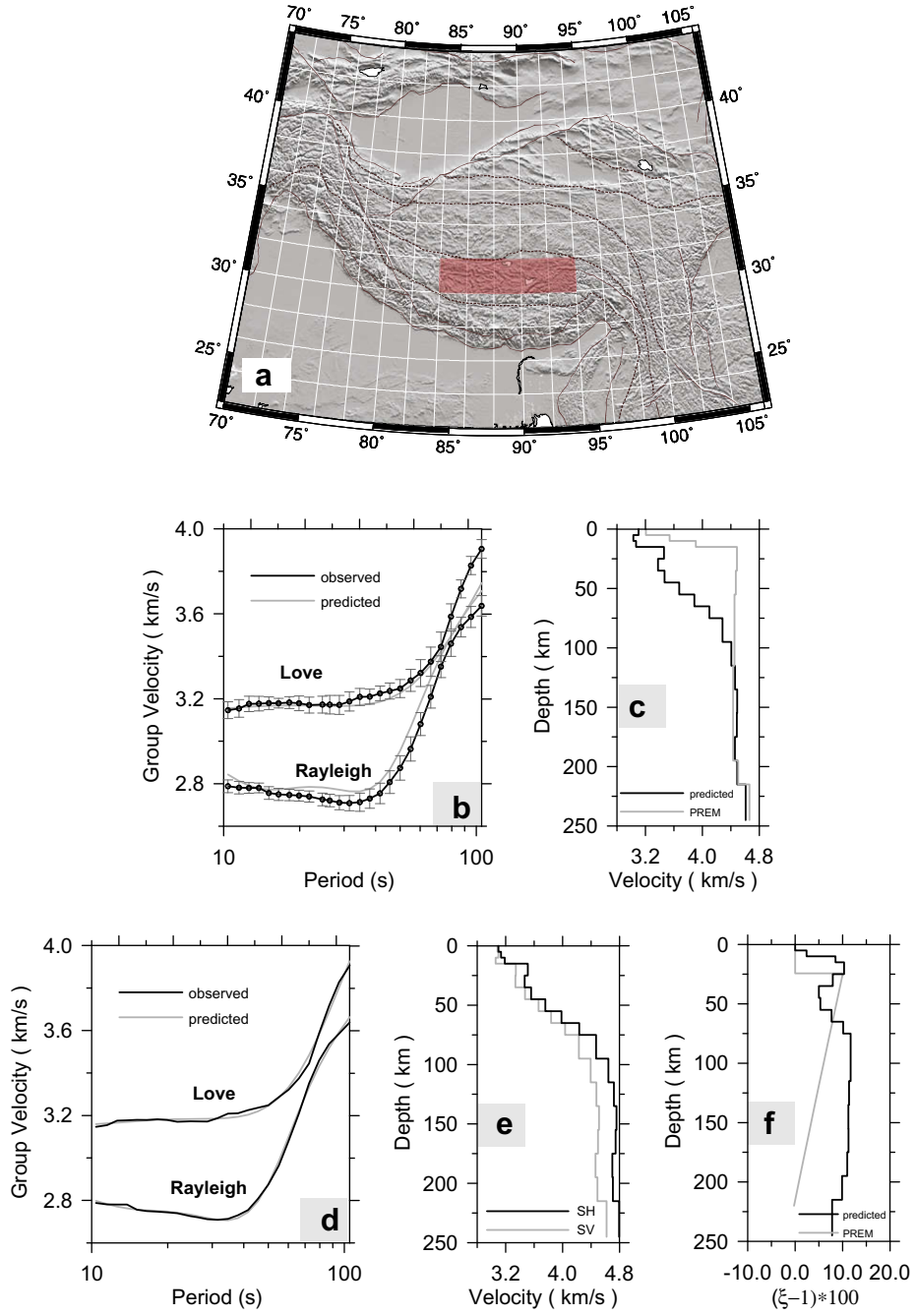

Fig. 4. Same legend as Fig. 3 but in relation to Lhasa Block.

formation. The crust–mantle models of isotropic shear-wave velocities can never simultaneously fit the observed Rayleigh and Love wave dispersion curves for the different Tibetan tectonic units: the Himalayan, Lhasa, Qiangtang, Songpan-Ganzi, and Kunlun-Qaidam Blocks (Figs. 3–7a–c). The differences between the group velocities calculated by forward modelling from the best-fitting isotropic models (Figs. 3–7c) and the observed group velocities determined by digital filtering (Figs. 3–7b) are most much lager than the measurement errors (<0.02 km/s) in the data and the standard deviations inferred from the group velocity variance on $2^\circ \times 2^\circ$ cells almost within the specific tectonic unit (Figs. 3–7a). However, when we consider different crust–mantle V_{SH} and V_{SV} velocity models (Figs. 3–7e) those differences almost completely disappear and both theoretical and observed group velocities show excellent agreement (Figs. 3–7d). Shapiro et al. (2004) reported the Tibetan middle crust requires the presence of relatively strong radial anisotropy according to the observed group-velocity dispersion. We infer the existence of radial anisotropy not only in the crust but also in the upper mantle from the clear L–R discrepancy shown by the V_{SH} and V_{SV} velocity models (Figs. 3–7e). To study the strength and spatial extent of radial anisotropy in Tibet from the L–R discrepancy, we have computed the strength by $(\xi - 1) * 100$ according to Silveira and Stutzmann (2002) with $\xi = (V_{SH}/V_{SV})^2$ (Lévêque et al., 1998; Debayle and Kennett, 2000; Maggi et al., 2006). The strength of radial anisotropy as a function of depth (Figs. 3–7f) is different from that obtained from the PREM model (Dziewonski and Anderson, 1981) assuming radial anisotropy for each tectonic unit, and also different from each other formation.

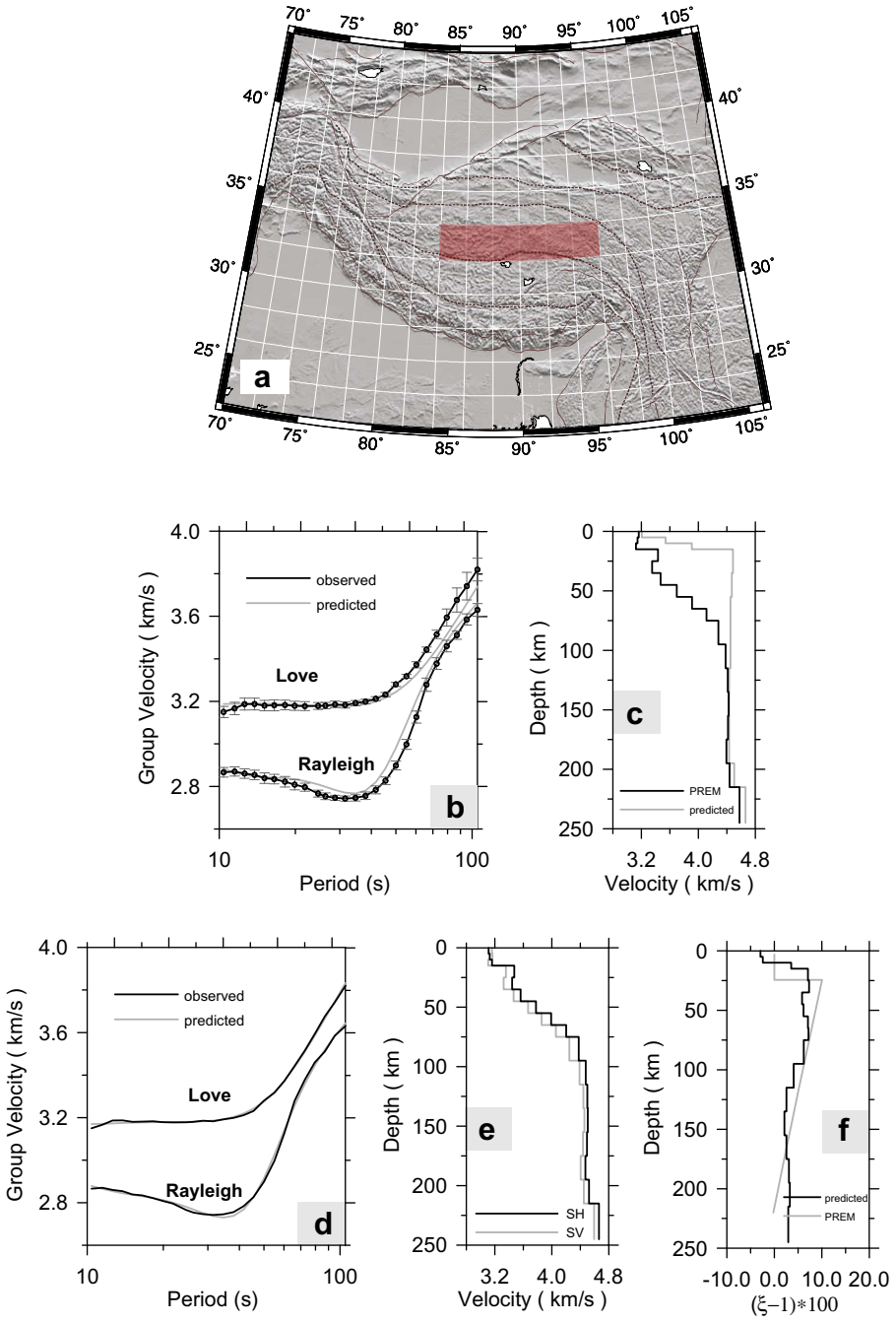

Fig. 5. Same legend as Fig. 3 but in relation to Qiangtang Block.

For the Himalayan Block strong radial anisotropy of about 7–10% with $V_{SH} > V_{SV}$ (Fig. 3e and f) is concentrated in the lower crust and uppermost mantle (45–100 km). At deeper depths 135–200 km the radial anisotropy is only 1.2% but reverse with $V_{SH} < V_{SV}$. For the Lhasa Block (Fig. 4e and f) strong radial anisotropy with $V_{SH} > V_{SV}$ is present not only in the middle crust (~9%, 15–35 km), but also in almost all the lithospheric mantle (~11%, 75–200 km), however, radial anisotropy with $V_{SH} < V_{SV}$ is not observed. For the Qiangtang Block (Fig. 5e and f) radial anisotropy of approximately 6% with $V_{SH} > V_{SV}$ is present within the depth interval 15–150 km, and radial anisotropy with $V_{SH} < V_{SV}$ is observed only in the shallowest 15 km where it is ~2%. For the Songpan-Ganzi Block (Fig. 6e and f) radial anisotropy of about 4.2% with $V_{SH} < V_{SV}$ affects the shallowest layer of 20 km, whereas radial anisotropy of ~5% with $V_{SH} > V_{SV}$ is present from 25 to 190 km, the maximum value being ~6% at the crust–upper mantle transition zone (70–90 km). For the Kunlun-Qaidam Block (Fig. 7e and f) radial anisotropy of approximately −7.5% with $V_{SH} < V_{SV}$ is observed only in the shallowest 10 km, but radial anisotropy with $V_{SH} > V_{SV}$ is present not only in the middle and lower crust (~5.6%, 10–35 km; ~2.0%, 35–55 km), but also in almost all the lithospheric mantle (8.5–10%, 55–95 km; ~5.3%, 95–115 km).

4. Radial anisotropy patterns

Fig. 8 displays the strength and spatial distribution of radial anisotropy down to 170 km as horizontal depth sections or maps of percentage anisotropy. Fig. 9 displays radial anisotropy patterns

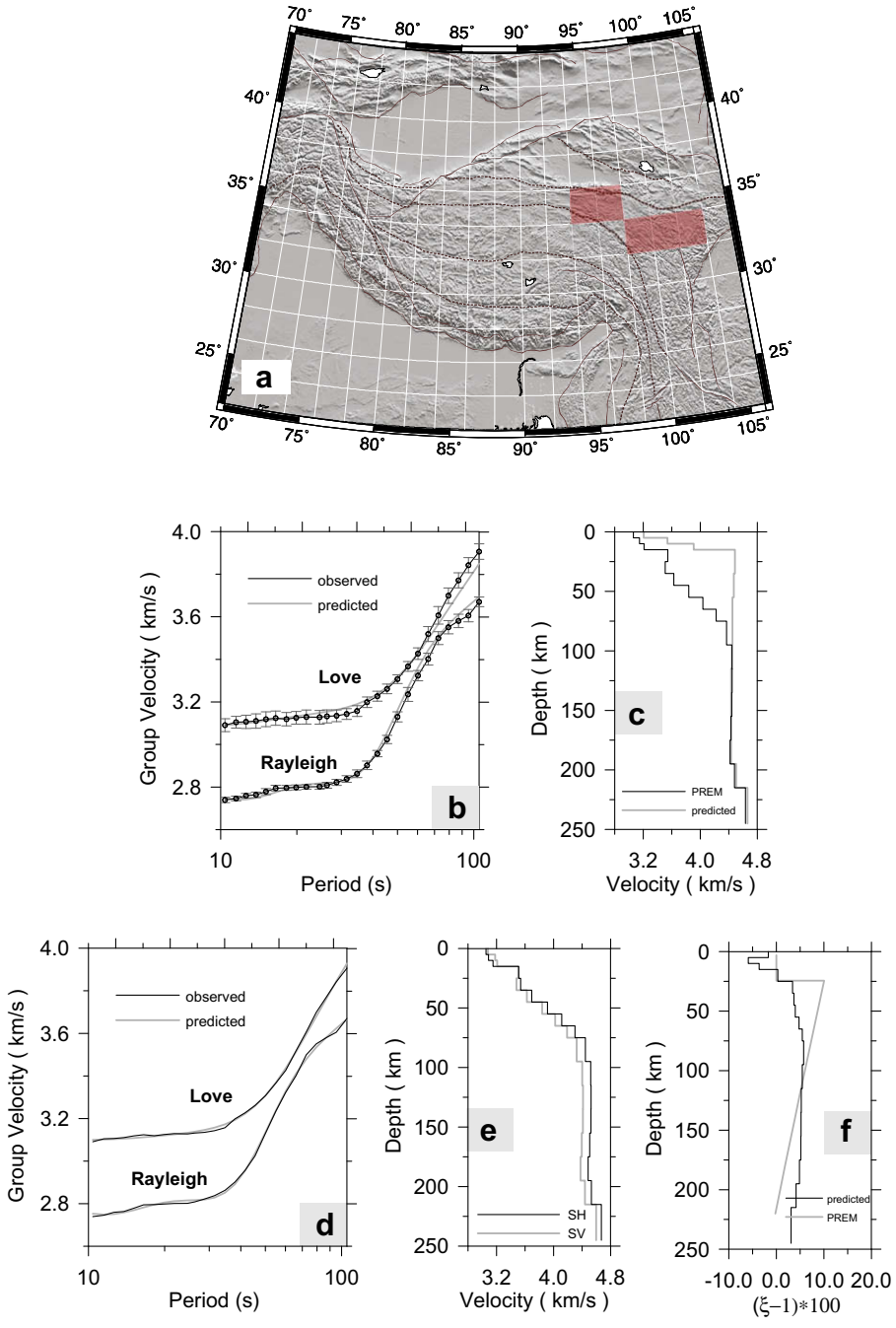

Fig. 6. Same legend as Fig. 3 but in relation to Songpan-Ganzi Block.

as vertical cross-sections along the five profiles outlined in Figs. 1 and 8. Three of these, A–A′, B–B′, C–C′, respectively cross western, central and eastern Tibet in the north-south direction at 83°E, 91°E and 99°E of longitude. The other two profiles, D–D′ and E–E′, cross the Qiangtang and Lhasa blocks in the east-west direction at 33°N and 31°N of latitude. In all cases the strength of radial anisotropy is computed by means of the expression $(\xi - 1) * 100$ according to Silveira and Stutzmann (2002) with $\xi = (V_{SH}/V_{SV})^2$ too. Fig. 10 depicts the average radial anisotropy as a function of the depth in our target area compared to that derived from the PREM model assuming anisotropy. The strength of average radial anisotropy with $V_{SH} > V_{SV}$ is comparatively smaller than the anisotropy provided by the PREM model. Our result has a similar trend although it is affected by a shift toward negative values, which is consistent with continental interiors and young orogens (Silver, 1996; Savage, 1999; Meissner et al., 2002; Fouch and Rondenay, 2006; Conrad et al., 2007).

The maps of radial anisotropy show some correlations with the geologic and tectonic features at depths down to around 100 km, and a close association between surface deformation and crust/mantle anisotropy can be established in the test region. At the depth of 8 km the image displays radial anisotropy with $V_{SV} > V_{SH}$ associated with the major sedimentary basins, such as Tarim Basin, Qaidam Basin and central Myanmar, and parts of other blocks, such as the central and eastern Himalaya. At this depth radial anisotropy with $V_{SH} > V_{SV}$ is associated with Tien Shan, Western Himalayan Syntaxes and most of the areas of the plateau. At depths of 18–35 km, the radial anisotropy clearly changes. The

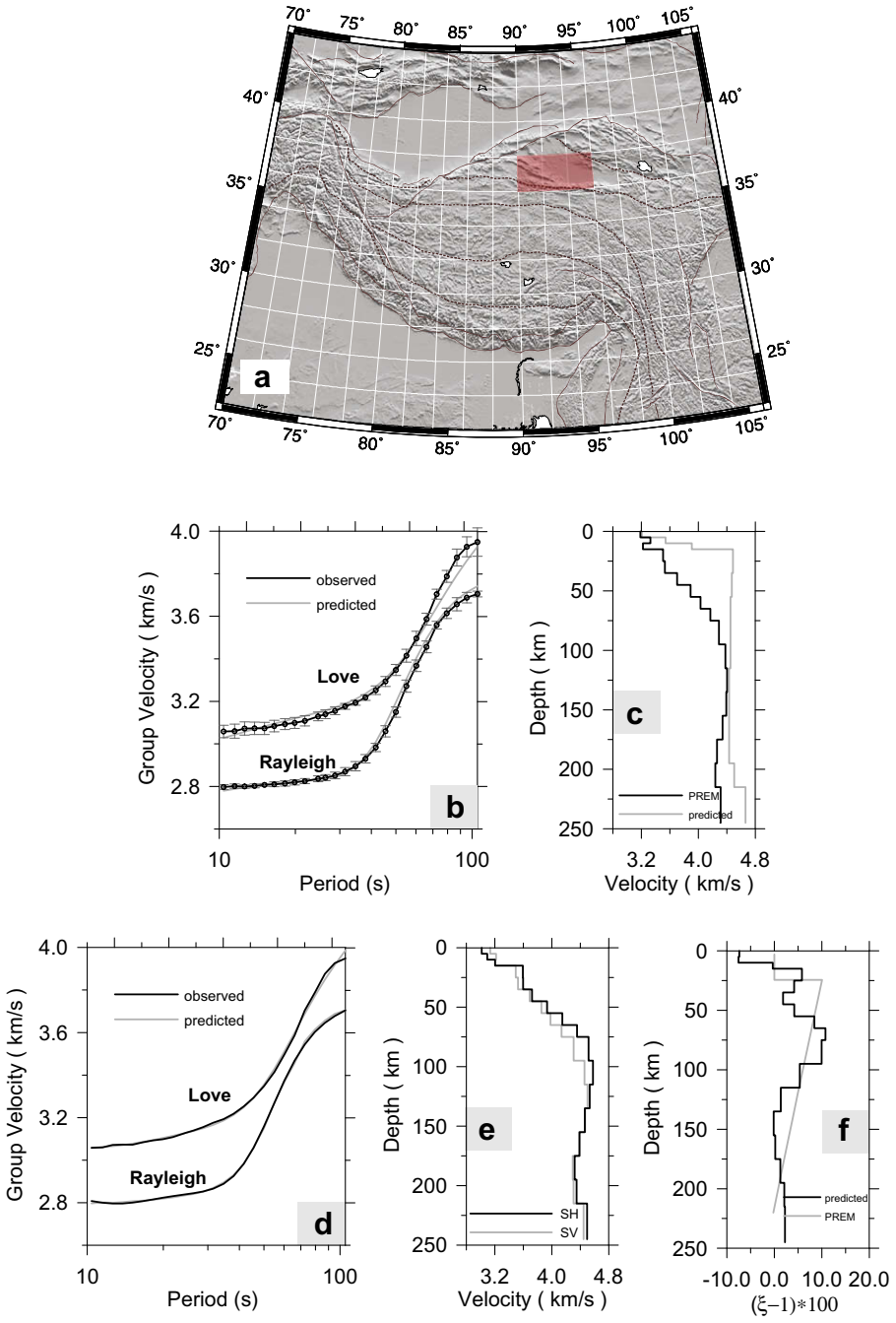

Fig. 7. Same legend as Fig. 3 but in relation to Kunlun-Qaidam Block.

zone underlying the Tarim Basin, and to the south of Eastern Himalayan Syntaxes (EHS), which including Burma Arc and Indochina Block, switch from being prominent areas of radial anisotropy with $V_{SH} < V_{SV}$ to one of radial anisotropy with $V_{SH} > V_{SV}$ (8–10%). At increasing depths 55–90 km, the images display radial anisotropy with $V_{SH} > V_{SV}$ to a great extent, but two notable zones with $V_{SH} < V_{SV}$ can be observed: the first is beneath Tarim Basin and areas to its south, and the other underlies the north-eastern

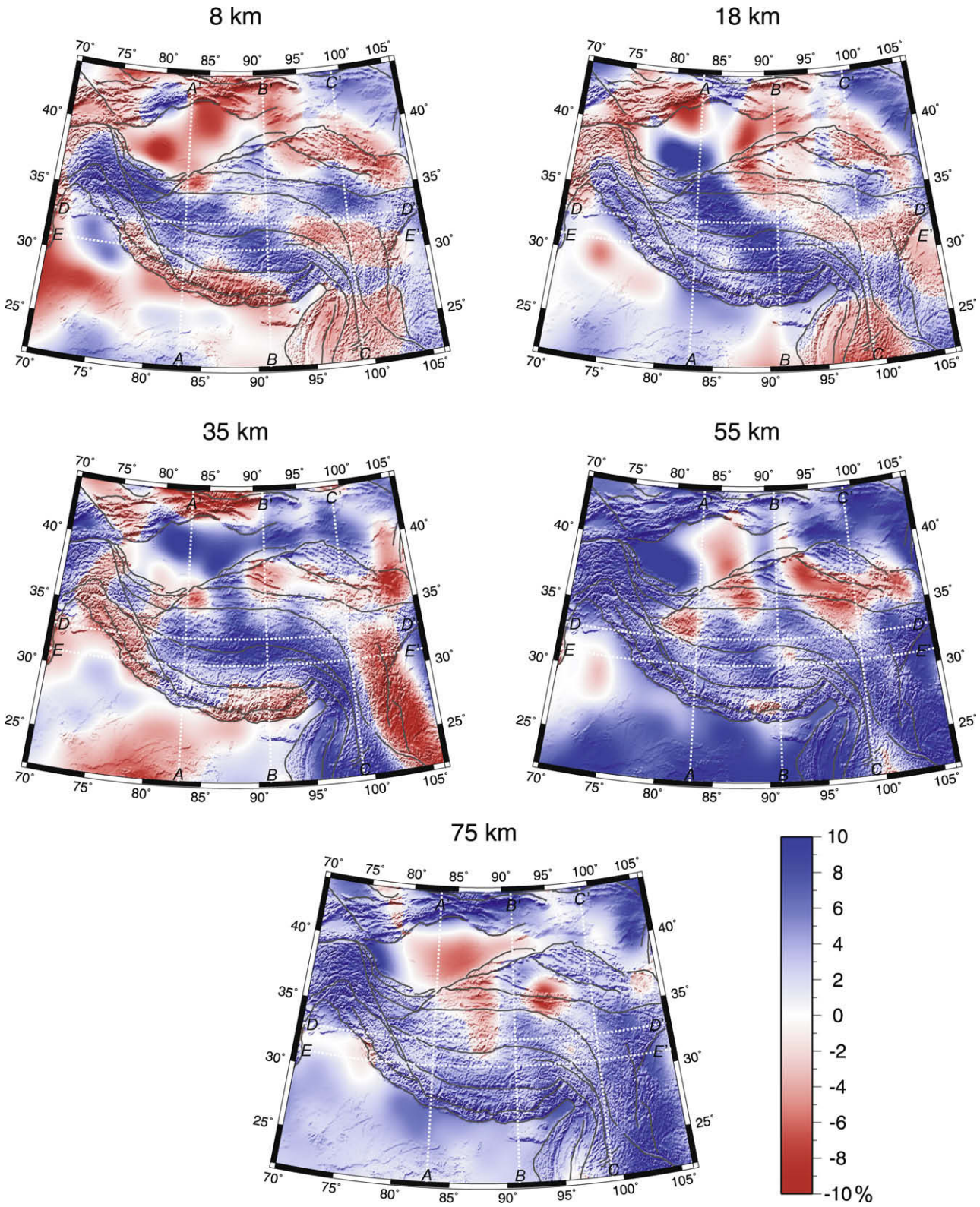

Fig. 8. Radial anisotropy maps estimated from the Love–Rayleigh discrepancy at several depths. In all cases the strength of radial anisotropy is computed by means of the expression $(\xi - 1) * 100$, with $\xi = (V_{SH}/V_{SV})^2$ at certain depth. Three N–S transects A–A′, B–B′, and C–C′, and two E–W profiles D–D′ and E–E′ indicate the locations of the vertical cross-sections shown in Figs. 1 and 9.

margin of the plateau. Especially, the former is increasing until it up to the most magnitude (−6% to −8%) at depth of ~90 km, while the latter is decreasing gradually and is disappeared completely at the depth of ~90 km too. However, at increasing depths more than 110 km the anisotropy picture initially depicted reappears again largely. Anyhow, in the depth range 8–110 km, the most conspicuous feature associated with the plateau is the large-scale anisotropy with $V_{SH} > V_{SV}$, that reaches ~10% successively at depths of 35–55 km, and 90–110 km, which then decreases gradually and switches to be slightly negative ($V_{SH} < V_{SV}$) in the depth more than 130 km.

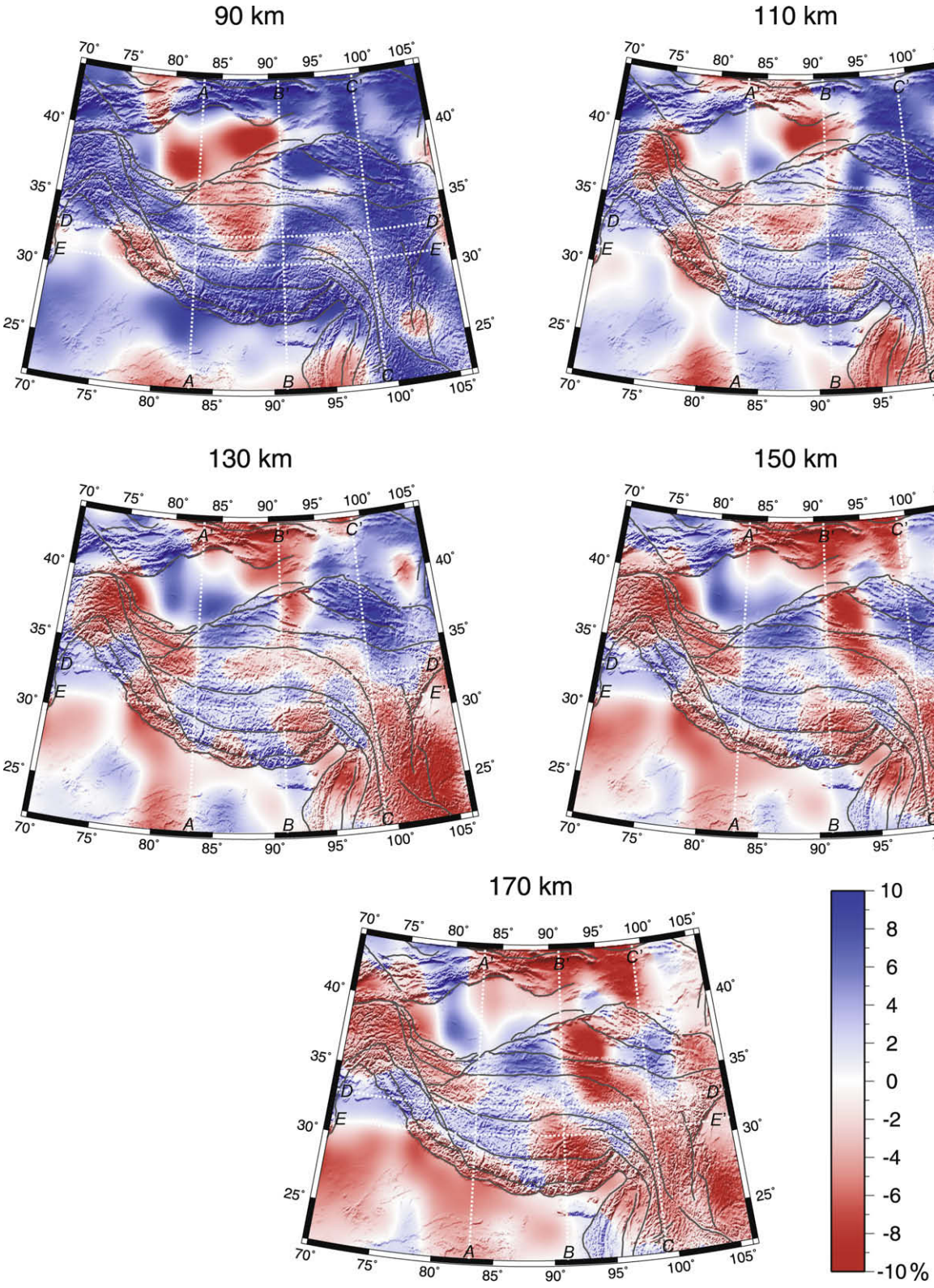

Fig. 8. (*continued*)

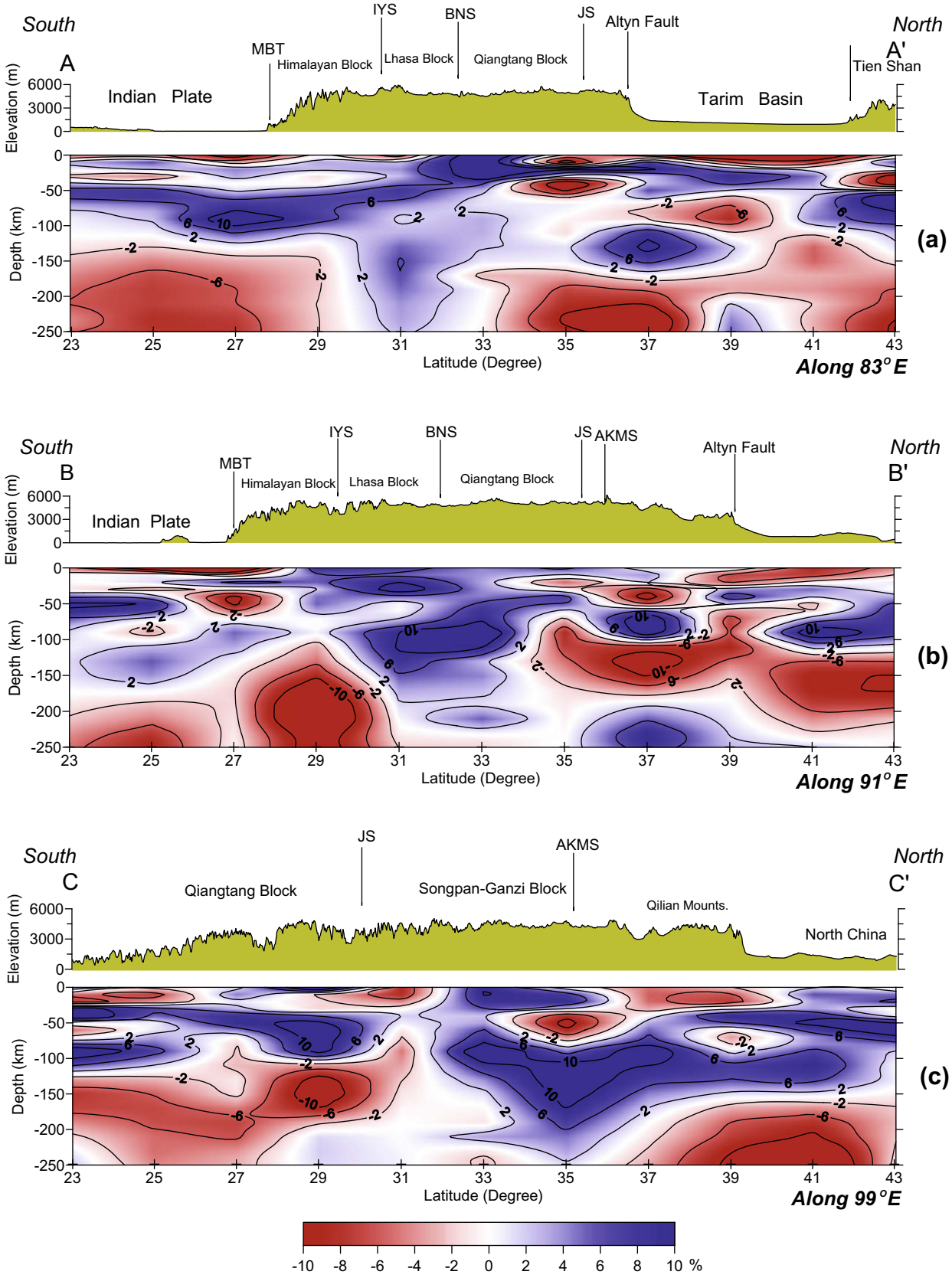

Fig. 9. Strength and spatial extent of radial anisotropy along the three N–S transects (a–c) and two W–E profiles (d and e) indicated in Figs. 1 and 8: (a) transect along 83°E; (b) transect along 91°E; (c) transect along 99°E; (d) profile along 33°N; (e) profile along 31°N. As before, the strength of radial anisotropy is computed from $(\xi - 1) * 100$, with $\xi = (V_{SH}/V_{SV})^2$ referred to a vertical cross section. The topographic relief [taken from the GTOPO30 digital elevation model (DEM), US Geological Survey, 1993], the names of the crossed physiographic regions and the boundaries intersected by the profiles have been added on top of the sections. To ensure clarity in the representations of the crust–upper mantle structures, the anisotropy contour lines were drawn at a step of 4%.

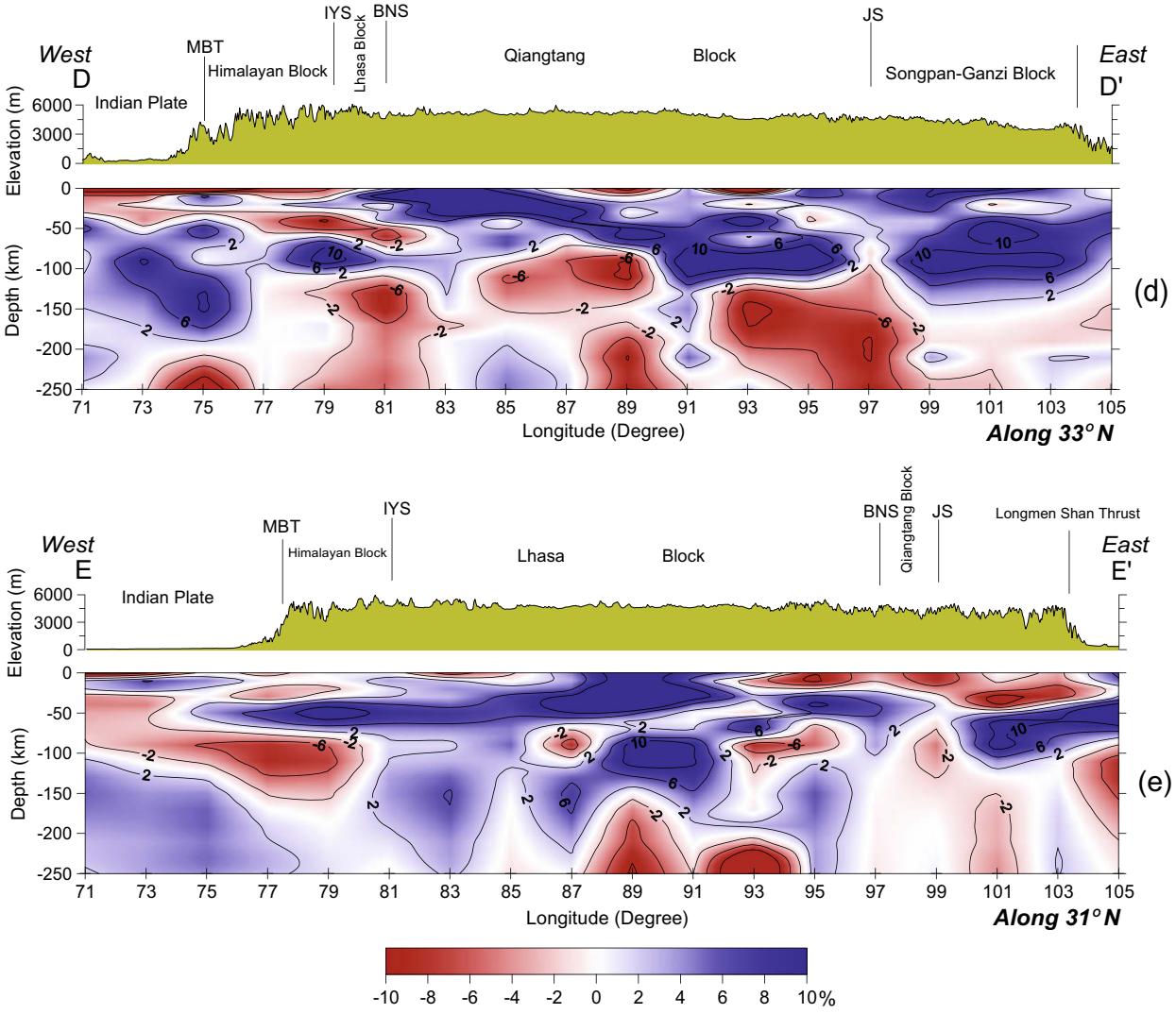

Fig. 9. (*continued*)

The profile A–A′ (Fig. 9a, along 83° east longitude) crosses from south to north the Indian Plate, Himalayan Block, Lhasa Block, Qiangtang Block and Tarim Basin and reaches Tien Shan. Below the Indian Plate the pattern of anisotropy is rather simple becoming more complex northward. Nevertheless, the most conspicuous feature is the existence of radial anisotropy with $V_{SH} > V_{SV}$ underlying most of the plateau with an average value of ~5%, that increases to ~10% at relatively shallow depths beneath the Qiangtang Block, and anisotropy with $V_{SH} > V_{SV}$ extending below the Lhasa Block down to 250 km.

The transect B–B′ (Fig. 9b, along 91° east longitude) crosses from south to north the Indian Plate, Himalayan Block, Lhasa Block, Qiangtang Block, the western end of Qaidam Basin and reaches the Altyn Fault. Radial anisotropy with $V_{SH} > V_{SV}$ of up to 6% extends mainly below the Lhasa and Qiangtang blocks. Two large zones of radial anisotropy with $V_{SH} < V_{SV}$ can be observed, the first to the south at depths greater than 150 km beneath the Himalayan Block (up to −10%), and the second to the north at depths 120–190 km between the Jinsha Suture (JS) and the Altyn Fault (up to −10% too).

The transect C–C′ (Fig. 9c, along 99° east longitude) crosses from south to north the Qiangtang Block, Songpan-Ganzi Block, the Qilian Mountains and reaches North China. The largest area of radial anisotropy with $V_{SH} > V_{SV}$ of up to 10% underlies the Songpan-Ganzi Block and part of the Qilian Mountains at depths greater than 80 km. Going from west to east (A–A′ → B–B′ → C–C′), a clear and gradual shift of radial anisotropy with $V_{SH} > V_{SV}$ takes place northward following the curved leading-edge of convergence between India and Tibet.

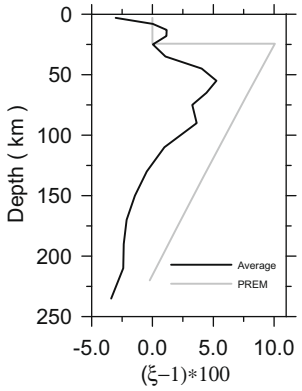

Fig. 10. Average radial anisotropy $(\xi - 1) * 100$ as a function of the depth (black line) in the Himalayan–Tibetan area compared to that derived from the anisotropic PREM model (grey line).

The two remaining west-to-east vertical sections cross the Qiangtang (Fig. 9d, along 33° north latitude) and Lhasa (Fig. 9e, along 31° north latitude) blocks. Radial anisotropy with $V_{SH} > V_{SV}$ of up to 6% underneath the Lhasa Block is the most remarkable feature, going to the east a different picture emerges in which we have radial anisotropy with $V_{SH} < V_{SV}$ up to −4% beneath the Qiangtang Block, but radial anisotropy with $V_{SH} > V_{SV}$ up to 8% beneath the eastern half of Qiangtang Block and the whole Songpan-Ganzi Block, which provides a view of the differential movement of the subducted lithosphere.

5. Discussion and conclusions

Theoretically, there is a trade-off between anisotropy and lateral heterogeneity (Levshin and Ratnikova, 1984; Yanovskaya et al., 1998), and the lateral heterogeneity of the medium along a surface wave path-length of a few hundred of kilometres may be certainly strong (Raykova and Nikolova, 2003). Fortunately, Silveira and Stutzmann (2002) utilized synthetic tests to show the validity of the regionalization method with sufficient path coverage as we used here to retrieve lateral velocity variation and radial anisotropy as a function of depth. Anyhow, as Shapiro et al. (2004) reported, the significant discrepancies in SH- and SV-velocity (Figs. 3–7d) may be attributed to radial anisotropy of the medium likely.

Besides surface waves, there are other seismological methods to ascertain the anisotropic property of the Earth's interior. These include shear-wave splitting analysis, receiver functions, P or S-wave relative arrival/delay times, and *Pn* anisotropy (Fouch and Rondenay, 2006). In particular, starting in the late 1980s, many studies based on teleseismic shear-wave splitting were performed to retrieve the seismic anisotropy beneath Tibet (McNamara et al., 1994; Hirn et al., 1995; Huang et al., 2000; Ozacar and Zandt, 2004), and comprehensive reviews of these studies were given by Silver (1996), Lavé et al. (1996) and Savage (1999). These papers reveal some outstanding features for different Tibetan blocks: the anisotropy derived from shear-wave splitting in the Himalayan Block is weak; in the Lhasa Block, it is weak or moderate splitting except at the northernmost edge of the block; although it is strong in the Qiangtang Block and still more so in the Songpan-Ganzi Block; to the northeast, in the Kunlun-Qaidam Block, it is moderate just like the central of the Lhasa Block; but to the northwest, in the Pakistan Himalayas, little splitting of *SKS* phase is measured. Our results for depth-dependent radial anisotropy for the main Tibetan blocks (Figs. 3–7f) show that:

(a) strong anisotropy (7–10%) with $V_{SH} > V_{SV}$ in the lower crust and uppermost mantle (45–100 km) in the Himalayan Block (Fig. 3f);
(b) the Lhasa Block has strongest anisotropy in the middle crust (∼9%) and almost all the lithospheric mantle (∼11%) (Fig. 4f);
(c) in the Qiangtang Block the strength of radial anisotropy is relatively strong (∼6%) in the middle crust and uppermost mantle (Fig. 5f);
(d) in the Songpan-Ganzi Block the anisotropy is rather weak (less than 5%), but stable within the lower crust and almost all the lithospheric mantle (Fig. 6f);
(e) in the Kunlun-Qaidam Block the strength of radial anisotropy is moderate in the middle crust (∼5.5%), but changes to strongest within the uppermost mantle (∼8.5%) (Fig. 7f);
(f) furthermore, looking at the spatial distribution maps, we see that the radial anisotropy ($V_{SH} > V_{SV}$ or $V_{SH} < V_{SV}$) beneath the Pakistan Himalayas (Fig. 8) is generally strong and of remarkable strength at all the checked depths.

Radial anisotropy as derived from surface waves is usually interpreted in terms of transverse isotropy with a vertical symmetry axis (VTI). In contrast, the anisotropy coming from shear-wave splitting is interpreted in terms of transverse isotropy with a horizontal symmetry axis (HTI). Under the simplest assumption of the VTI, the area with strong radial anisotropy should be the one with weak or no splitting. Comparing both types of anisotropy on the basis of L–R discrepancy or shear-wave splitting, the results concerning the Tibetan blocks are partially consistent with this rule. For example, in Pakistan Himalayas and Lhasa Block both exhibit very strong radial anisotropy but little or weak splitting anisotropy, which maybe indicates that these locations are candidates for possible near-vertical orientation of α axes (Savage, 1999). However, in the Qiangtang Block both strong radial anisotropy and obvious shear-wave splitting are measured, which could be combined to get a model with orthorhombic symmetry (Savage, 1999; Priestley et al., 2006). Anyhow, the splitting measurements represent vertically integrated point measurements, whereas surface waves average horizontally over large distances, a direct comparison is worthy of care usually (Fouch and Rondenay, 2006).

Non-uniqueness, arguable resolution and smoothing introduced at different stages, are all constraints which impinge upon the inversion process of surface wave data. We can only discuss large-scale radial anisotropy variations both laterally and with depth that are well constrained by path density and azimuthal coverage, and conclude on the main features of the crust and upper mantle. Areas beneath the Tibetan Plateau in which radial anisotropy exists in excess of 6% radial anisotropy are found in the crust and upper mantle underlying most of the plateau, even in some places the radial anisotropy reaches 10% (Fig. 9). The strength and spatial configuration of radial anisotropy in the plateau is the result of the stress/strain state characterized by a regime of horizontal compressive forces in the frame of the convergence of the Indian and Asian plates, accompanied by the actions induced by the subduction of the Indian plate beneath Asia. The maximum strength is focused on the Lhasa and Qiangtang blocks in the western and central parts of the plateau (Fig. 9a and b), and also on the Songpan-Ganzi Block in the eastern part of the plateau (Fig. 9c). This correlates with the subducted lithosphere especially beneath the eastern end of the Jinsha Suture (JS) that again appears like the curved front of the junction between India and Tibet (Chen et al., 2009). From the north-south cross-sections, the anisotropy patterns suggest a style of coherent deformation caused by the compressive driving forces interacting with the Indian and the Asian plates. From the west-to-east cross-sections, the Lhasa Block with significant widespread radial anisotropy (Fig. 9e) supports this deformational style. In contrast the Qiangtang Block is associated with an asymmetrical pattern of radial anisotropy (Fig. 9d). The predominant anisotropy with $V_{SH} > V_{SV}$ is 8–10% at depth $\leqslant$50 km on its western half (also underlying the Lhasa Block), and approximately 6–10% at depths 50–125 km on its eastern half (also underlying the Songpan-Ganzi Block). This seems to indicate the lateral variation of the lithospheric rheology and a differential movement as regards the compressive driving forces.

Acknowledgments

We are indebted to the data processing centres CDSN in China and IRIS in the United States for the facilities given for data acquisition. Helpful comments, suggestions and criticism from two anonymous referees that led to significant improvement of the early manuscript are gratefully acknowledged. Most of the graphic illustrations were generated with the Generic Mapping Tools (GMT) software by Wessel and Smith. The National Natural Science Foundation of China (Grant 40504012), the Ministry of Science and

Technology of China (Grant 2002CB412604), and the Knowledge Innovation Program of the Chinese Academy of Sciences supported this research. The present work takes advantage of the Collaboration Agreement between the Institute of Geology and Geophysics, Chinese Academy of Sciences, and the University of Zaragoza, Spain.

References

Aki, K., Richards, P.G., 1980. Quantitative Seismology: Theory and Methods. W.H. Freeman, San Francisco.

Anderson, D., 1961. Elastic wave propagation in layered anisotropic media. Journal of Geophysical Research 66, 2953–2963.

Badal, J., Corchete, V., Payo, G., Canas, J.A., Pujades, L., Serón, F.J., 1990. Processing and inversion of long-period surface-wave data collected in the Iberian Peninsula. Geophysical Journal International 100, 193–202.

Badal, J., Corchete, V., Payo, G., Serón, F.J., Canas, J.A., Pujades, L., 1992. Deep structure of the Iberian Peninsula determined by Rayleigh wave velocity inversion. Geophysical Journal International 108, 71–88.

Chen, Y., Badal, J., Hu, J.F., 2009. Love and Rayleigh wave tomography of the Qinghai-Tibet Plateau. Pure and Applied Geophysics (in revision).

Conrad, C.P., Behn, M.D., Silver, P.G., 2007. Global mantle flow and the development of seismic anisotropy: differences between the oceanic and continental upper mantle. Journal of Geophysical Research 112, B07317. doi:10.1029/2006JB004608.

Debayle, E., Kennett, B.L.N., 2000. Anisotropy in the Australasian upper mantle form Love and Rayleigh waveform inversion. Earth and Planetary Science Letters 184, 339–351.

Dimri, V., 1992. Deconvolution and Inverse Theory, Application to Geophysical Problems. Elsevier, Amsterdam.

Dziewonski, A., Anderson, D., 1981. Preliminary reference earth model. Physics of the Earth and Planetary Interiors 25, 297–356.

Ekström, G., Dziewonski, A.M., 1998. The unique anisotropy of the Pacific upper mantle. Nature 394, 168–172.

Fouch, M.J., Rondenay, S., 2006. Seismic anisotropy beneath stable continental interiors. Physics of the Earth and Planetary Interiors 158, 292–320.

Herrmann, R.B., 2002. Computer Programs in Seismology, version 3.30. St. Louis University, Missouri.

Hirn, A., Jiang, M., Sapin, M., Diaz, J., Nercessian, A., Lu, Q.T., Lépine, J.C., Shi, D.N., Sachpazi, M., Pandey, M.R., 1995. Seismic anisotropy as an indicator of mantle flow beneath the Himalayas and Tibet. Nature 375, 571–574.

Huang, W., Ni, J.F., Tilmann, F., Nelson, D., Guo, J., Zhao, W., Mechie, J., Kind, R., Saul, J., Rapine, R., Hearn, T.M., 2000. Seismic polarization anisotropy beneath the central Tibetan Plateau. Journal of Geophysical Research 105 (B12), 27979–27989.

Huang, Z., Peng, Y., Luo, Y., Zheng, Y., Su, W., 2004. Azimuthal anisotropy of Rayleigh waves in East Asia. Geophysical Research Letters 31, L15617. doi:10.1029/2004GL020399.

Julià, J., Ammon, C.J., Herrmann, R.B., Correig, A.M., 2000. Joint inversion of receiver functions and surface wave dispersion observations. Geophysical Journal International 143, 99–112.

Lavé, J., Avouac, J.P., Lacassin, R., Tapponnier, P., Montagner, J.P., 1996. Seismic anisotropy beneath Tibet: evidence for eastward extrusion of the Tibetan lithosphere? Earth and Planetary Science Letters 140, 83–96.

Lev, E., Long, M.D., van der Hilst, R.D., 2006. Seismic anisotropy in Eastern Tibet from shear wave splitting reveals changes in lithospheric deformation. Earth and Planetary Science Letters 251, 293–304.

Lévêque, J.J., Debayle, E., Maupin, V., 1998. Anisotropy in the Indian Ocean upper mantle from Rayleigh- and Love-waveform inversion. Geophysical Journal International 133, 529–540.

Levshin, A., Ratnikova, L., 1984. Apparent anisotropy in inhomogeneous media. Geophysical Journal of Royal Astronomical Society 76, 65–69.

Maggi, A., Debayle, E., Priestley, K., Barruol, G., 2006. Azimuthal anisotropy of the pacific region. Earth and Planetary Science Letters 250, 53–71.

Marone, F., van der Lee, S., Giardini, D., 2004. Shallow anisotropy in the Mediterranean mantle from surface waves. Geophysical Research Letters 31, L06624. doi:10.1029/2003GL018948.

McNamara, D.E., Owens, T.J., Silver, P.G., Wu, F.T., 1994. Shear wave anisotropy beneath the Tibetan Plateau. Journal of Geophysical Research 99 (B7), 13655–13665.

Meissner, R., Mooney, W.D., Artemieva, I., 2002. Seismic anisotropy and mantle creep in young orogens. Geophysical Journal International 149, 1–14.

Montagner, J.-P., Jobert, N., 1988. Vectorial tomography, II: application to the Indian Ocean. Geophysical Journal of Royal Astronomical Society 94, 309–344.

Montagner, J.P., Tanimoto, T., 1990. Global anisotropy in the upper mantle inferred from the regionalization of phase velocities. Journal of Geophysical Research 95, 4797–4819.

Montagner, J.P., Tanimoto, T., 1991. Global upper mantle tomography of seismic velocities and anisotropies. Journal of Geophysical Research 96, 30337–30351.

Muyzert, E., Snieder, R., 2000. An alternative parameterisation for surface waves in a transverse isotropic medium. Physics of the Earth and Planetary Interiors 118, 125–133.

Ozacar, A.A., Zandt, G., 2004. Crustal seismic anisotropy in central Tibet: implications for deformational style and flow in the crust. Geophysical Research Letters 31, L23601. doi:10.1029/2004GL021096.

Park, J., Levin, V., 2002. Seismic anisotropy: tracing plate dynamics in the mantle. Science 296 (19), 485–489.

Pasyanos, M.E., Walter, W.R., 2001. A surface wave dispersion study of the Middle East and North Africa for monitoring the comprehensive Nuclear-Test-Ban Treaty. Pure and Applied Geophysics 158, 1445–1474.

Priestley, K., Debayle, E., Mckenzie, D., Pilidou, S., 2006. Upper mantle structure of eastern Asia from multimode surface waveform tomography. Journal of Geophysical Research 111, B10304. doi:10.1029/2005JB004082.

Rapine, R., Tilmann, F., West, M., Ni, J., 2003. Crustal structure of northern and southern Tibet from surface wave dispersion analysis. Journal of Geophysical Research 108 (B2), 2120. doi:10.1029/2001JB000445.

Raykova, R.B., Nikolova, S.B., 2003. Anisotropy in the earth's crust and uppermost mantle in southeastern Europe obtained from Rayleigh and Love surface waves. Journal of Applied Geophysics 54, 247–256.

Ribe, N.M., 1989. Seismic anisotropy and mantle flow. Journal of Geophysical Research 94, 4213–4223.

Ritzwoller, M.H., Levshin, A.L., 1998. Eurasian surface wave tomography: group velocities. Journal of Geophysical Research 103 (B3), 4839–4878.

Ritzwoller, M.H., Shapiro, N.M., Levshin, A.L., Leahy, G.M., 2001. Crustal and upper mantle structure beneath Antarctica and the surrounding oceans. Journal of Geophysical Research 106, 30645–30670.

Russell, D.R., 1987. Multi-channel processing of dispersed surface waves. PhD Thesis, Saint Louis University, Missouri.

Savage, M.K., 1999. Seismic anisotropy and mantle deformation: what have we learned from shear wave splitting? Reviews of Geophysics 37 (1), 65–106.

Shapiro, N.M., Ritzwoller, M.H., 2002. Monte-Carlo inversion for a global shear-velocity model of the crust and upper mantle. Journal of Geophysical Research 151, 88–105.

Shapiro, N.M., Ritzwoller, M.H., Molnar, P., Levin, V., 2004. Thinning and flow of Tibetan crust constrained by seismic anisotropy. Science 305 (9), 233–236.

Silveira, G., Stutzmann, E., 2002. Anisotropic tomography of the Atlantic Ocean. Physics of the Earth and Planetary Interiors 132, 237–248.

Silveira, G., Stutzmann, E., Griot, D., Montagner, J.-P., Victor, L.M., 1998. Anisotropic tomography of the Atlantic Ocean from Rayleigh surface waves. Physics of the Earth and Planetary Interiors 106, 257–273.

Silver, P.G., 1996. Seismic anisotropy beneath the continents: probing the depths of geology. Annual Review of Earth and Planetary Sciences 24, 385–432.

Song, Z.H., An, C.Q., Chen, G.Y., Chen, L.H., Zhuang, Z., Fu, Z.W., Lu, Z.L., Hu, J.F., 1991. Study on 3D velocity structure and anisotropy beneath west China from Love wave dispersion. Chinese Journal of Geophysics 34 (6), 694–707 (in Chinese).

Villaseñor, A., Ritzwoller, M.H., Levshin, A.L., Barmin, M.P., Engdahl, E.R., Spakman, W., Trampert, J., 2001. Shear velocity structure of central Eurasia from inversion of surface wave velocities. Physics of the Earth and Planetary Interiors 123, 169–184.

Vuan, A., Robertson Maurice, S.D., Wiens, D.A., Panza, G.F., 2005. Crustal and upper mantle S-wave velocity structure beneath the Bransfield Strait (West Antarctica) from regional surface wave tomography. Tectonophysics 397, 241–259.

Yanovskaya, T.B., Kizima, E.S., Antonova, L.M., 1998. Structure of the crust in the Black Sea and adjoining regions from surface wave data. Journal of Seismology 2, 303–316.

Yin, A., Harrison, T.M., 2000. Geologic evolution of the Himalayan–Tibetan orogen. Annual Review of Earth and Planetary Sciences 28, 211–280.